Ultra-Fast Laser Pulses as a Probe of Electron Dynamics: A Next Generation QTAIM Perspective

Huan He[1], Xiao Peng Mi[1], Xinjie Zhou[1], Genwei Hong[1], Tianlv Xu[1], Herbert Früchtl[2], Tanja van Mourik[2], Martin, J. Paterson[3], Steven R. Kirk[*1] and Samantha Jenkins[*1]

[1]Key Laboratory of Chemical Biology and Traditional Chinese Medicine Research and Key Laboratory of Resource National and Local Joint Engineering Laboratory for New Petro-chemical Materials and Fine Utilization of Resources, College of Chemistry and Chemical Engineering, Hunan Normal University, Changsha, Hunan 410081, China
[2]EaStCHEM School of Chemistry, University of Saint Andrews, North Haugh, St Andrews, Fife KY16 9ST, Scotland, United Kingdom.
[3]Institute of Chemical Sciences, School of Engineering and Physical Sciences, Heriot-Watt University, Edinburgh, EH14 4AS, UK

email: steven.kirk@cantab.net
email: samanthajsuman@gmail.com

We investigate the construction of an ultra-fast laser probe to determine the response of the electron dynamics of ethane using next generation QTAIM (NG-QTAIM). This is undertaken by applying a pair of simulated left and right circularly polarized ultra-fast laser pulses of duration 10 femtoseconds. A proportional increase in the C-C *BCP* bond strain with peak electric field was discovered. NG-QTAIM was used to identify a characteristic morphology associated with ultra-fast laser probes. Candidate ultra-fast laser probes were selected on the basis of the ground state population remaining undisturbed at a time $t = 15$ fs.

1. Introduction

Ultra-fast optics is an emerging field that requires new analysis tools designed for ultra-fast (femtosecond) timescales[1]. This requirement implies using the electron charge density distribution $\rho(\mathbf{r})$ rather than differences in atomic positions which move on orders of magnitude slower time scales. Experiments by Beaulieu *et al.* were undertaken on neutral molecules that utilized the coherent helical motion of bound electrons[2]. For example, the relationship between steric and electronic factors was recently discovered to be more complex[3] than previously understood discernable from inspection of molecular structures for the helical electronic transitions of spiroconjugated molecules[4,5]. Ethane was earlier used in an investigation with next generation QTAIM (NG-QTAIM) interpretation of an achiral molecule[6]. Recently, ethane was used with third generation eigenvector trajectories, using ultra-fast non-ionizing laser pulses [7]. This enabled the analysis of the mechanical and chiral properties of the electron dynamics of ethane without needing to subject the C-C bond to torsions of the H-C1-C2-H dihedral angles as was the case for second-generation eigenvector-trajectories[5]. In another recent investigation NG-QTAIM was used to quantify the effect on the electron dynamics of an ethene molecule of a simulated linearly polarized non-ionizing ultra-fast laser pulse of 20 femtosecond duration with a peak amplitude electric-field $\pm\mathbf{E} = 200\text{x}10^{-4}$ a.u.[8]. The goals of the earlier investigation on ethane included determining the effect of the laser pulse on the electron dynamics in terms of the mechanical properties of bond-twisting, bond-flexing as well as the chiral character of left-handed counter-clockwise (CCW [-1]) and right-handed clockwise (CW [+1]) direction of an applied circularly polarized ultra-fast laser pulse. The goal of this investigation is to explore optimal laser pulse 'probes' that comprise a trade-off between minimal disruption of the superposition of states and the numerical accuracy of the NG-QTAIM analysis. Such a probe will be useful for optimal control.

In this investigation we determine the use of ultra-fast laser pulses as probes of the electron dynamics of ethane using third-generation eigenvector-following trajectories $\mathbb{T}_{\mathbf{F}}(s)$ within NG-QTAIM[7,9,10], see the theoretical background section for further details. We will investigate the use of a simulated ultra-fast laser pulse of 10 femtoseconds (fs) duration to define an ultra-fast laser 'probe' of the NG-QTAIM properties, as close as possible, of the relaxed ethane. We will again use a pair of right-handed (R, [+1]) and left-handed (L, [-1]) circularly polarized laser pulses for the *yz* plane, see **Scheme 1**. This search for ultra-fast laser pulse probes will be undertaking by selecting candidate ultra-fast laser probes to locate the minimum peak electric-field $\pm\mathbf{E}$ strength selected from $\mathbf{E} = 1.0\text{x}10^{-4}$ au, $\mathbf{E} = 2.0\text{x}10^{-4}$ au, $\mathbf{E} = 5.0\text{x}10^{-4}$ au, $\mathbf{E} = 10.0 \text{ x } 10^{-4}$ a.u., where the molecule remains almost entirely in the ground state 15 fs after the pulse has ended. The numerical accuracy of the candidate ultra-fast probes will also be considered, i.e. ensuring the peak E-field is still sufficient to yield numerical significant values of the NG-QTAIM properties.

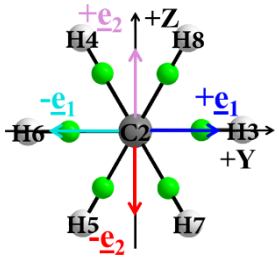

Scheme 1. The molecular graphs of ethane indicating the *yz* plane of the applied circularly polarized ultra-fast laser pulse. The most ($\pm\underline{\mathbf{e}}_2$) and least ($\pm\underline{\mathbf{e}}_1$) preferred eigenvector directions of the total charge density accumulation $\rho(\mathbf{r}_b)$ at the C1-C2 bond critical point (*BCP*) are represented by green spheres.

An additional 'non-probe' pair of left and right circularly polarized laser pulses with a larger **E**-field (**E** = 200.0 x 10^{-4} a.u.) is also included in this investigation. This larger value of peak **E**-field is included to demonstrate that the short 10 fs laser pulse is sufficiently long for a mixture of excited states with significant populations to be induced.

2. Theoretical Background

The background of QTAIM and next generation QTAIM (NG-QTAIM)[9–17] is provided in the **Supplementary Materials S1**, including the procedure to generate the Hessian of $\rho(\mathbf{r})$ eigenvector-*following* trajectories $\mathbb{T}_F(s)$ and the $\mathbb{U}$-space distortion set $\{\mathbb{F},\mathbb{T},\mathbb{A}\}$. Note the use of the subscript "$_F$" to denote eigenvector-following trajectories $\mathbb{T}_F(\boldsymbol{s})$ which are created using laser irradiation and not bond torsions as was the case for second-generation trajectories.

The $\pm\underline{\mathbf{e}}_1$ and $\pm\underline{\mathbf{e}}_2$ eigenvectors lie in the *yz* plane of polarization, see **Scheme 1**. Note that the $\pm\underline{\mathbf{e}}_2$ eigenvector corresponds to the most *facile*, i.e. easier, *direction* for displacement of the *BCP* electrons when the *BCP* is torsioned. In the $\mathbb{U}$-space distortion set $\{\mathbb{F},\mathbb{T},\mathbb{A}\}$ the bond-flexing $\mathbb{F}$, defined as $\mathbb{F} = [(\underline{\mathbf{e}}_1\cdot\mathbf{dr})_{max}]_{CW} - [(\underline{\mathbf{e}}_1\cdot\mathbf{dr})_{max}]_{CCW}$, provides a measure of the 'flexing-strain' that a bond-path is under when subjected to an external force such as an **E**-field or a circularly polarized laser pulse. The intermediate results for the $\mathbb{U}$-space distortion sets are provided in the **Supplementary Materials S4**.

The bond-twist $\mathbb{T}$ is defined as the difference in the maximum projections (the dot product of the Hessian of $\rho(\mathbf{r})$ $\underline{\mathbf{e}}_2$ eigenvector and the *BCP* displacement **dr**) of the $\mathbb{T}_F(s)$ values between the left-handed circularly polarized (L, CCW [+1]) and right-handed circularly polarized (CW [-1]) laser pulse: $\mathbb{T} = [(\underline{\mathbf{e}}_2\cdot\mathbf{dr})_{max}]_{CW} - [(\underline{\mathbf{e}}_2\cdot\mathbf{dr})_{max}]_{CCW}$. The bond-twist $\mathbb{T}$ quantifies the *circular* displacement of the C1-C2 *BCP* i.e., where the largest magnitude Hessian of $\rho(\mathbf{r})$ eigenvalue (λ_2) is associated with $\pm\underline{\mathbf{e}}_2$. The $\pm\underline{\mathbf{e}}_2$ corresponds to the direction in which the electrons at the *BCP* will be most easily displaced when the *BCP* is subjected to circular displacement i.e. torsion[18]. Note for

conventionally chiral molecules we use the variable chirality $\mathbb{C}$ instead of bond-twist $\mathbb{T}$, however, the form of the expression $[(\underline{\mathbf{e}}_2 \cdot \mathbf{dr})_{max}]_{CW} - [(\underline{\mathbf{e}}_2 \cdot \mathbf{dr})_{max}]_{CCW}$ is the same.

The bond-axiality $\mathbb{A}$ is defined as $\mathbb{A} = [(\underline{\mathbf{e}}_3 \cdot \mathbf{dr})_{max}]_{CW} - [(\underline{\mathbf{e}}_3 \cdot \mathbf{dr})_{max}]_{CCW}$; this quantifies the direction of *axial* displacement of the bond critical point (*BCP*) in response to the left-handed (CCW [-1]) and right-handed (CW [+1]) circularly polarized laser pulses, i.e. the sliding of the *BCP* along the bond-path[19]. The twist-helicity function $\mathbb{T}_{helicity} = \mathbb{T}|\mathbb{A}|$, i.e., the numerical product of the bond-twist and the magnitude of the bond-axiality $\mathbb{A}$, can be used to determine the nature of any chiral behaviors present in ethane in the absence or presence of a circularly polarized laser pulse. A value of $\mathbb{T}_{helicity} \approx 0$ was previously discovered for ethane using second-generation eigenvector trajectories and characterizes conventional achiral molecules [5].

3. Computational Details

The geometry of the ethane molecule was first optimized in zero applied external electric (**E**) field. Pseudo-CI (configuration interaction) singles eigenvectors were then built using a set of configuration state functions, using the hybrid linear response time-dependent density functional theory/configuration interaction (LR-TDDFT/CI) approach described in detail in previous work[20–22]. Both the geometry optimization and the construction of the configuration state functions were carried out using TD-DFT at the CAM-B3LYP[23] /aug-cc-pVTZ[24,25] level using the Gaussian G09 v.E.01[26] package. This choice of basis set and functional has been shown elsewhere in the literature[27] to provide accurate descriptions of excited states. The fifty lowest-energy excited states were computed using an 'ultrafine' integration grid and no symmetry constraints. A linear combination of the singly-excited configuration state functions was used to construct each time-independent many-electron state. Using the time-dependent CI implementation in the detCI module[20,21] within the ORBKIT[28] package, a 'library' of transition dipole moments between states was precomputed and saved. This 'library' was then later used in the propagation of the electron dynamics.

The electron dynamics was then propagated within the 'clamped nuclei' approximation, with the wavefunction being propagated as a linear complex-weighted sum of the previously computed pseudo-CI singles states, as described in previous work[20,21]. Modelling of the physical effect of the laser pulse driving out-of-equilibrium polarization in the electron density distribution can be carried out using a number of methods, including the 'real-time TD-DFT', also known as 'time-dependent Kohn-Sham', methods of Zhu *et al*. [29,30]. The alternative hybrid (TD-DFT/TDCI) approach used in this work, previously described by Tremblay *et al*. [31,32] can, in particular, make use of the CI-singles states, energies and transition dipole moments computed by any quantum chemistry code and also takes account of state-mixing, implicitly required to describe propagation of the laser-induced superposition state. In this hybrid (TD-DFT/TDCI) approach, using the many-electron time dependent Schrödinger equation, the field-free Hamiltonian is used, along with the additional semi-classical dipole

interaction approximation term $-\boldsymbol{\mu}.\mathbf{E}(t)$, where the dot indicates a vector dot product, $\boldsymbol{\mu}$ is the dipole operator and $\mathbf{E}(t)$ is the time-dependent applied electric field vector. The pre-computed dipole moment library, evaluated using the aforementioned transition densities, was used at each dynamics time-step to calculate the dipole interaction term $-\boldsymbol{\mu}.\mathbf{E}(t)$ and the electron dynamics were propagated for a total of 25 fs in the 'interaction' representation.

The electric field **E** components as a function of time were precomputed and tabulated at 10,000 equally-spaced times from t = 0 fs to t = 10 fs. The time-dependent CI dynamics calculation then computed the instantaneous field at any given dynamics timestep within the duration of the ultra-fast laser pulse by cubic-spline interpolation from these precomputed values.

A 'field broadening' approach was employed: for a '$\sin^2$' amplitude envelope function pulse of duration ΔT the energetic broadening of the field is simply $\Delta E = \hbar/\Delta T$. Low-lying electronic states are usually well-separated energetically, so only very short pulses, such as the 10 fs pulse used here, are broad enough to excite the desired superposition states. As short pulses are inherently energetically broad, they are also inevitably unselective. Therefore a laser carrier frequency (excitation energy) of ω = 0.350 a.u. was chosen to span a relatively wide range of the lower-lying excited states. More selective strategies for excitation of superposition states are still an active research topic in the literature, e.g. 'undertuning' and 'overtuning' strategies have had only partial success [33], although laser-induced selective alignment of molecules relative to fields is now experimentally feasible [34,35].

The electron dynamics was propagated using a dynamics timestep of 2.158236×10^{-4} fs, chosen to yield exactly 2012 dynamics timesteps per cycle of the chosen laser carrier frequency (excitation energy) with ω = 0.350 a.u. This magnitude of timestep and number of timesteps per cycle was found in previous work [7] to provide good accuracy for the Runge-Kutta integration of the electron dynamics within the 'detCI' code. The overall dynamics propagation time was 25fs [115836 timesteps]. Populations of the time-varying multi-reference ground |0> and excited states |1> , |2>, |3>, ... |20> quantifying the content of the superposition state were recorded every 20 dynamics timesteps. These populations were confirmed to preserve overall normalization during the entire dynamics simulation. A 'timeslice' was defined within the dynamics run, corresponding to two full cycles of the laser excitation frequency, centered on the 'peak' of the laser pulse at t = 5fs i.e., exactly midway through the 10 fs laser pulse, with one full field cycle on either side of t = 5fs. The CRITIC2 code[36] with the 'density-smoothing'[37] option was used to obtain the bond critical points (*BCP*s), bond paths and eigenvectors of the Hessian of the total electronic charge density $\rho(\mathbf{r})$ for each snapshot within the 'timeslice'. Additional checks were made ensuring that the Poincaré-Hopf relationship was satisfied in all cases. NG-QTAIM properties were obtained for the total electron density snapshots using the in-house QuantVec[38] suite, which is compatible with the output of the CRITIC2 code. Eigenvector-following NG-QTAIM trajectories were then calculated for each 'timeslice'.

The specification of the electric field, generation of the gridded total electronic charge density distribution $\boldsymbol{\rho(r)}$ and tabulated excitation frequencies ω are provided in the **Supplementary Materials S2**.

4. Results and discussions

The populations of the multi-reference superposition states of the candidate right-handed (**CW[+1]**) circularly polarized non-ionizing ultra-fast laser probes with peak **E**-fields of **E** = $1.0\text{x}10^{-4}$ a.u., **E** = $2.0\text{x}10^{-4}$ a.u., **E** = $5.0\text{x}10^{-4}$ a.u. and **E** = $10.0 \text{ x } 10^{-4}$ a.u. in the *yz* plane are presented in **Figure 1(a-d)** respectively, see also **Scheme 1**. A larger peak **E**-field of $200.0\text{x}10^{-4}$ a.u. is also included where the mixture of electronic states comprises significant populations of the |4>, |6>, |7>, |9> and |12> excited states, see **Figure 1(e)**. The (**CW[+1]**) and (**CCW[-1]**) plots are indistinguishable and therefore the CCW plots are provided in the **Supplementary Materials S2**. The tabulated ethane excitation frequencies are also provided in the **Supplementary Materials S2**. Additional plots of the variation of the populations of the multi-reference superposition states for a selection of electric **E**-field values are provided in the **Supplementary Materials S3**.

The populations of the ground state at 15 fs, i.e., 5 fs after the end of the 10 fs ultra-fast laser probes, are presented in **Table 1**. Initial inspection of the population of 1.000 of the ground state indicates that a peak **E**-field of $1.0\text{ x}10^{-4}$ a.u. does not significantly populate any excited states at 15 fs after the application of the laser pulse, see **Table 1**. A decrease of the ground state population for the four candidate laser pulse probes, with peak **E**-fields of **E** = $1.0\text{x}10^{-4}$ a.u., **E** = $2.0\text{x}10^{-4}$ a.u., **E** = $5.0\text{x}10^{-4}$ a.u. and **E** = $10.0 \text{ x } 10^{-4}$ a.u., with increase in the peak **E**-field is observed. The value of 0.1134 of the ground state population at 15 fs for the non-probe laser pulse with peak **E**-field **E** = $200.0 \text{ x } 10^{-4}$ a.u. indicates significant contributions from the |4>, |6>, |7>, |9> and |12> excited states, see **Figure 1(e)**.

Table 1. Populations of the ground state at t = 15 fs for the ultra-fast right-handed (**CW[+1]**) circularly polarized laser probes.

Peak **E**-field (a.u.)	population of the ground state at t = 15 fs
$1.0\text{x}10^{-4}$	1.0000
$2.0\text{x}10^{-4}$	0.9997
$5.0\text{x}10^{-4}$	0.9984
$10.0\text{x}10^{-4}$	0.9936
$200.0\text{x}10^{-4}$	0.1134

The plots of the populations of the ground states for the candidate ultra-fast laser probes are indistinguishable, see **Figure 1**, therefore we will now consider the variations of the C1-C2 *BCP* ellipticity ε, see **Figure 2.**

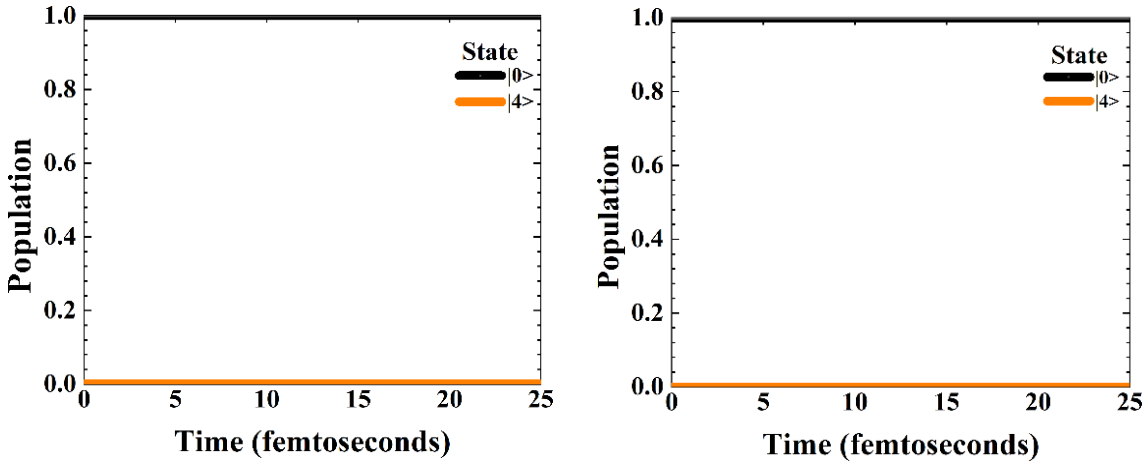

(a)

(b)

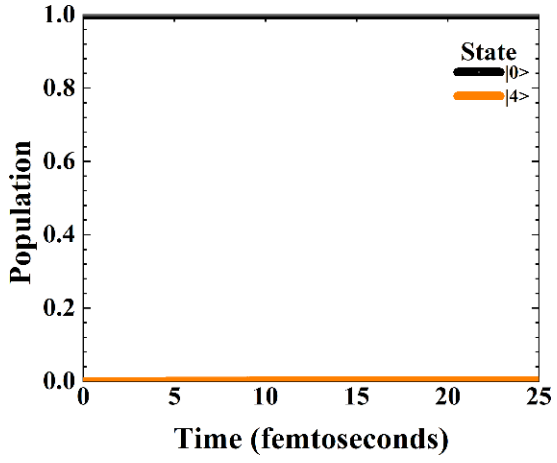

(c)

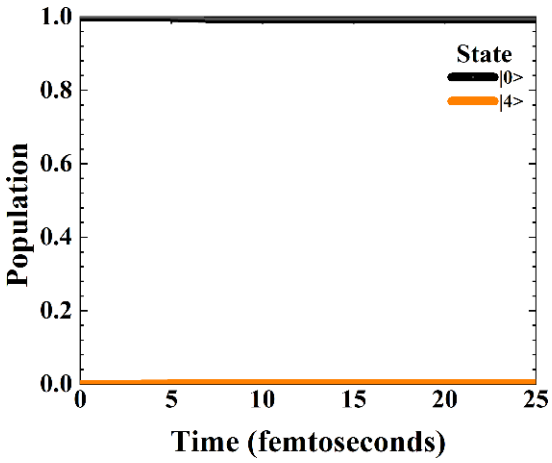

(d)

\

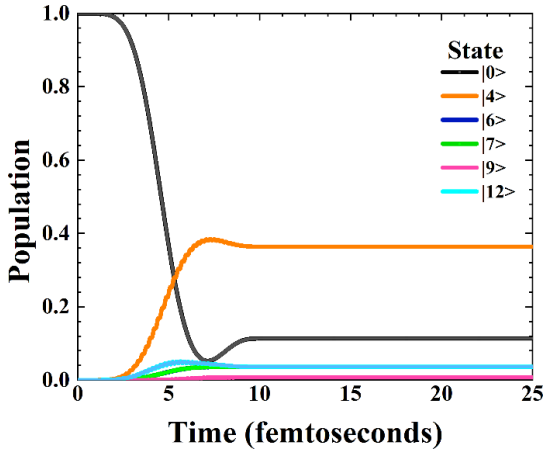

(e)

Figure 1. The variations of population with time of significantly populated electronic states for the right-handed clockwise (**CW[+1]**) and left-handed counter-clockwise (**CCW[-1]**) '$\sin^2$' shaped pulses, circularly polarized in the *yz*-plane at t = 10 fs with peak electric fields with values **E** = 1.0x10^{-4} a.u., **E** = 2.0x10^{-4} a.u., **E** = 5.0x10^{-4} a.u., **E** = 10.0x10^{-4} a.u. and **E** = 200.0x10^{-4} a.u. are presented in sub-figures **(a-e)** respectively. For further details also refer to the computational details and **Scheme 1**.

The effect of the right-handed (**CW[+1]**) and left-handed (**CCW[-1]**) circularly polarized laser pulse in the *yz* plane on the electron charge density distribution $\rho(\mathbf{r_b})$ at the C1-C2 *BCP* is considered using the variation of the C1-C2 *BCP* ellipticity ε, see **Figure 2**. Note, for comparison the same scale is used for all values of the peak **E**-field in the plots of C1-C2 *BCP* ellipticity ε. A proportionate increase in the amplitude of the variation of the C1-C2 *BCP* ellipticity ε is observed for all laser pulses, with the response of the lowest peak **E**-field of **E** = 1.0×10^{-4} a.u. being negligible on the scale chosen, see **Figure 2(a-e)**. The response to the candidate laser probe with the largest associated peak **E**-field (10.0×10^{-4} a.u.) is an order of magnitude lower than the non-probe pulse peak with a peak **E**-field of 200.0×10^{-4} a.u., compare **Figure 2(d)** and **Figure 2(e)**. The ethane C1-C2 *BCP* ellipticity ε however, does not provide a complete understanding of the response of $\rho(\mathbf{r_b})$ at the C1-C2 *BCP* to the ultra-fast lasers, due to the lack of full symmetry-breaking[9] as a result of the lack of consideration of the $\pm\underline{\mathbf{e}}_1$, $\pm\underline{\mathbf{e}}_2$ and $\pm\underline{\mathbf{e}}_3$ eigenvectors.

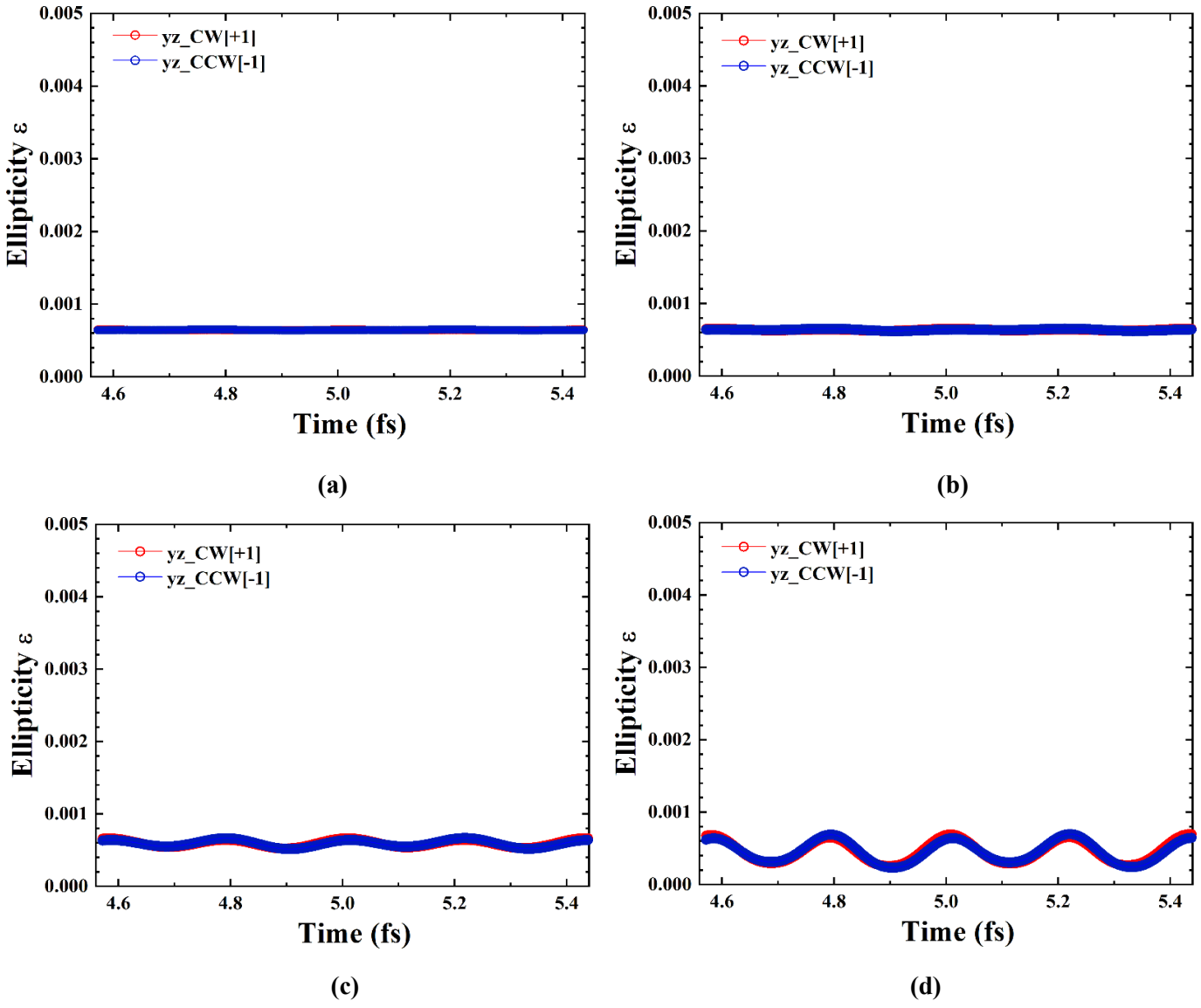

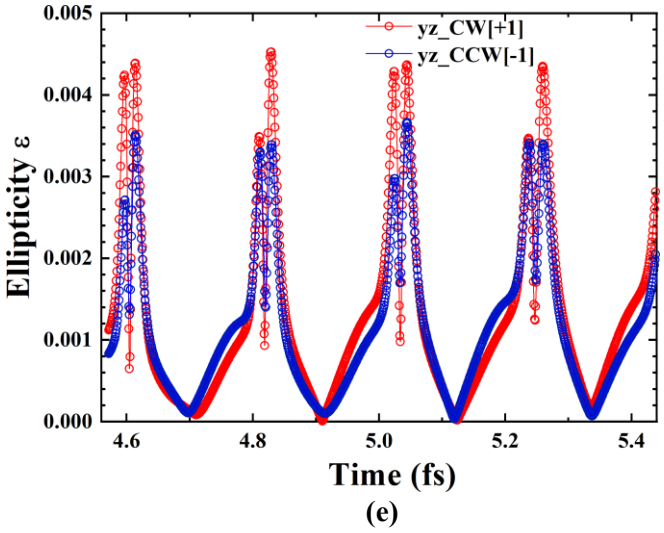

Figure 2. The variation of the ethane C1-C2 *BCP* ellipticity ε for the right-handed (**CW[+1]**) and left-handed (**CCW[-1]**) circularly polarized in the *yz* plane with peak **E**-fields, **E** = 1.0 x10^{-4} a.u., 2.0x10^{-4} a.u., 5.0x10^{-4} a.u., 10.0x10^{-4} a.u. and 200.0x10^{-4} a.u. are presented in sub-figures **(a-e)** respectively. For further details refer to the computational details, **Scheme 1** and **Figure 1**.

A limitation of using the C1-C2 *BCP* ellipticity ε for understanding the response of the $\rho(\mathbf{r_b})$ to the applied ultra-fast laser pulses is the lack of physical basis. To overcome this limitation, the circularly polarized ultra-fast laser generated Hession of $\rho(\mathbf{r})$ eigenvector-following trajectories $\mathbb{T}_{\mathbf{F}}(s)$ will be used to analyze the response of the electron dynamics, see **Figure 3**. All of the $\mathbb{T}_{\mathbf{F}}(s)$ in this investigation are smooth and continuous. The $\mathbb{T}_{\mathbf{F}}(s)$ of the candidate laser probes possess simple tightly wrapped morphologies, see **Figure 3(a-d)** in contrast to the complex loosely wrapped morphologies of the $\mathbb{T}_{\mathbf{F}}(s)$ corresponding to the large peak **E**-field, see **Figure 3(e)**.

The values of the bond-flexing $\mathbb{F}$ approximately increase with peak **E**-field for all values of the peak **E**-field, however, the corresponding values of the bond-twist $\mathbb{T}$ only increase approximately with peak **E**-field values of **E** = 2.0 x10^{-4} a.u. or greater. In contrast, values of the bond-axiality $\mathbb{A}$, which comprise the twist-helicity $\mathbb{T}_{helicity} = \mathbb{T}|\mathbb{A}|$, are found to be insignificant in all cases of the peak **E**-field, see **Table 2**.

Table 2. The variation of the C1-C2 *BCP* $\mathbb{U}$-space distortion sets $\{\mathbb{F}, \mathbb{T}, \mathbb{A}\}$ comprising the bond-flexing $\mathbb{F}$, bond-twist $\mathbb{T}$ and bond-axiality $\mathbb{A}$, with application of a pair of right-handed (**CW[+1**]) and left-handed (**CCW[-1**]) circularly polarized laser pulses of duration 10 fs with peak electric field intensity **E** in units of 10^{-4} a.u. in the *yz* plane. The twist-helicity function $\mathbb{T}_{helicity} = \mathbb{T}x|\mathbb{A}|$. Note, the value of the twist-helicity function $\mathbb{T}_{helicity} = 0$ in all cases.

Electric field **E**	$\{\mathbb{F}, \mathbb{T}, \mathbb{A}\}$
1.0×10^{-4} au	{0.00000023, -0.00000069, 0.00000095}
2.0×10^{-4} au	{0.00000327, -0.00000068, 0.00000029}
5.0×10^{-4} au	{0.00001067, 0.00000262, -0.00000757}
10.0×10^{-4} au	{0.00001913, 0.00000487, -0.00000001}
200.0×10^{-4} au	{0.00329274, 0.00257559, 0.00000230}

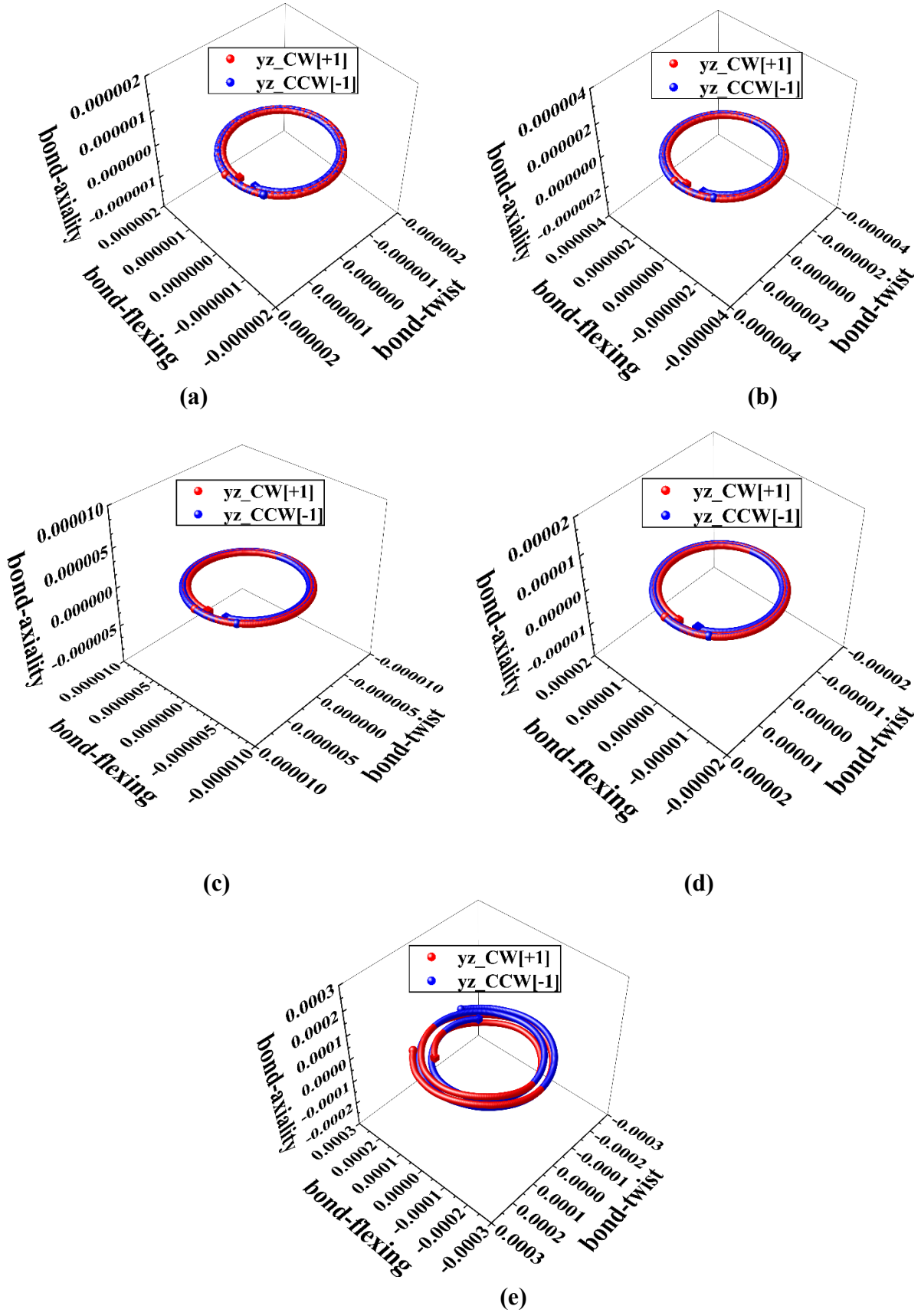

Figure 3. The ethane C1-C2 *BCP* Hessian of $\rho(\mathbf{r})$ eigenvector-following trajectories $\mathbb{T}_F(s)$ for the right-handed, clockwise (**CW[+1]**) and left-handed, counter-clockwise (**CCW[-1]**) circularly polarized laser pulses in the *yz* plane corresponding to the electric field **E** = 1.0 x 10^{-4} a.u., **E** = 2.0 x 10^{-4} a.u., **E** = 5.0 x 10^{-4} a.u., **E** = 10.0 x 10^{-4} a.u. and **E** = 200.0 x 10^{-4} a.u. are presented in sub-figures **(a-e)** respectively.

5. Conclusions

In this investigation we explored the construction of an ultra-fast laser pulse of duration 10 fs to act as a 'probe' applied to understand the electron dynamics of ethane. This was undertaken by choosing a selection of candidate simulated left clockwise (**CW[+1]**) and right counter-clockwise (**CCW[-1]**) circularly polarized ultra-fast laser probes with peak **E**-fields of 1.0 x 10^{-4} a.u., 2.0 x 10^{-4} a.u., 5.0 x 10^{-4} a.u. and 10.0 x 10^{-4} a.u. The criterion for choosing the candidate ultra-fast laser probes was that the populations of the ground state at time t = 15 fs for these pulses was as high as possible. The resulting populations of the ground state at time t = 15 fs for the candidate probes were found to be in the range from 1.000 down to 0.9936. An additional non-probe pair of laser pulses with a larger **E**-field (**E** = 200.0 x 10^{-4} a.u.) was chosen and demonstrated that the very short 10 fs laser pulse was sufficiently long for a mixture of excited states with a ground state population of only 0.1134.

We quantified the response of the electron dynamics to the circularly polarized laser pulses of the scalar C1-C2 *BCP* ellipticity ε. The choice the best value for the peak **E**-field as the laser probe was not fully informed by consideration of the variations of the ellipticity ε with time. This is because the ellipticity ε is a scalar measure that does not provide any physical vector-based indicator of the ideal choice(s) of ultra-laser probe.

The C1-C2 *BCP* Hessian of $\rho(\mathbf{r})$ eigenvector-following trajectories $\mathbb{T}_{\mathbf{F}}(s)$ with the $\mathbb{U}$-space distortion set $\{\mathbb{F},\mathbb{T},\mathbb{A}\}$ revealed and quantified the complete absence of chiral character, determined from the value of the twist-helicity function $\mathbb{T}_{helicity} = 0$ for all values of the peak **E**-field, in line with expectations of a conventionally achiral molecule and our previous investigation of ethane[7].

The use of the vector-based Hessian of $\rho(\mathbf{r})$ eigenvector-following trajectories $\mathbb{T}_{\mathbf{F}}(s)$, however, provided information about the $\mathbb{U}$-space distortion set $\{\mathbb{F},\mathbb{T},\mathbb{A}\}$ to better inform the probe selection. This is to enable the best possible trade-off between minimal disturbance of the electron dynamics of the superposition of states and the maximum accuracy of the $\mathbb{U}$-space distortion set $\{\mathbb{F},\mathbb{T},\mathbb{A}\}$.

The contrasting effect of the laser probe using (very low) peak **E**-fields (**E** = 1.0 x 10^{-4} a.u., 2.0 x 10^{-4} a.u., 5.0 x 10^{-4} a.u. and 10.0 x 10^{-4} a.u.) and high peak **E**-field (**E** = 200.0 x 10^{-4} a.u.) on the electron dynamics is visualized by the $\mathbb{T}_{\mathbf{F}}(s)$. The significant disturbance induced by the high peak **E**-field is apparent by the loose wrapping of $\mathbb{T}_{\mathbf{F}}(s)$ which has a complex morphology in contrast to the tightly wrapped $\mathbb{T}_{\mathbf{F}}(s)$ and simple morphology associated with the very low peak **E**-field laser probes. Therefore, we suggest that the tightly wrapping simple morphology observed for the $\mathbb{T}_{\mathbf{F}}(s)$ corresponding to the very low peak **E**-fields is characteristic of laser probes. The loose wrapping of the $\mathbb{T}_{\mathbf{F}}(s)$ with the high peak **E**-field indicates a high degree of disruption of the electron dynamics and therefore this **E**-field is completely unsuitable for use as a laser probe.

The best choice of ultra-fast laser as a probe may therefore be a peak **E**-field of 5.0 x 10^{-4} a.u. Future planned

work includes using ultra-fast lasers as probes and NG-QTAIM to investigate chiral molecules, to understand how ultra-fast lasers may influence chiral, achiral and mixed chiral/achiral character [39]. In particular, on much longer timescales, namely after laser-induced nuclear rearrangements have occurred, a final pair of non-ionizing left and right circularly polarized ultra-fast low intensity laser pulses will be used to generate a probe $\mathbb{T}_{\mathbf{F}}(s)$ again.

In addition, the laser carrier envelope phase difference will be varied to induce different time dependent mixtures of excited states. Other areas of application include the solid state e.g. superconductivity induced by higher intensity ultra-fast left and right circularly polarized laser pulses, informed by the Fermi energy. The subsequent effects on the electron dynamics will be determined by the laser probes, informed by NG-QTAIM, introduced in this investigation.

The optimal ultra-fast laser probe information obtained using NG-QTAIM in this investigation is important because of its application to optical control and will be suitable for use with relatively large molecules.

Conflict of Interests Statement

The authors have no conflict of interests to declare.

Funding Information

The Hunan Natural Science Foundation of China project gratefully acknowledged approval number: 2022JJ30029. The One Hundred Talents Foundation of Hunan Province is also gratefully acknowledged for the support of S.J. and S.R.K. MJP thanks the EPSRC for funding through grants EP/T021675 and EP/V006746.

The use of SHARCNET computing facilities is acknowledged through the auspices of our sponsor Paul W. Ayers.

References

[1] D.T. Reid, C.M. Heyl, R.R. Thomson, R. Trebino, G. Steinmeyer, H.H. Fielding, R. Holzwarth, Z. Zhang, P. Del'Haye, T. Südmeyer, G. Mourou, T. Tajima, D. Faccio, F.J.M. Harren, G. Cerullo, Roadmap on ultrafast optics, J. Opt. 18 (2016) 093006. https://doi.org/10.1088/2040-8978/18/9/093006.

[2] S. Beaulieu, A. Comby, D. Descamps, B. Fabre, G.A. Garcia, R. Géneaux, A.G. Harvey, F. Légaré, Z. Mašín, L. Nahon, A.F. Ordonez, S. Petit, B. Pons, Y. Mairesse, O. Smirnova, V. Blanchet, Photoexcitation circular dichroism in chiral molecules, Nature Phys. 14 (2018) 484–489. https://doi.org/10.1038/s41567-017-0038-z.

[3] K.C. Harper, M.S. Sigman, Three-Dimensional Correlation of Steric and Electronic Free Energy Relationships Guides Asymmetric Propargylation, Science. 333 (2011) 10.1039/D1CC01904J. https://doi.org/10.1126/science. 1206997.

[4] M.H. Garner, C. Corminboeuf, Helical electronic transitions of spiroconjugated molecules, Chem. Commun. 57 (2021) 10.1002/qua.26884. https://doi.org/10.1039/D1CC01904J.

[5] H. Xing, A. Azizi, R. Momen, T. Xu, S.R. Kirk, S. Jenkins, Chirality–helicity of cumulenes: A non-scalar charge density derived perspective, Int. J. Quantum Chem. 122 (2022) e26884. https://doi.org/10.1002/qua.26884.

[6] Z. Li, T. Xu, H. Früchtl, T. van Mourik, S.R. Kirk, S. Jenkins, Chiral and steric effects in ethane: A next generation QTAIM interpretation, Chem. Phys. Lett. 800 (2022) 139669. https://doi.org/10.1016/j.cplett.2022.139669.
[7] X.P. Mi, H. Lu, T. Xu, H. Früchtl, T. van Mourik, M.J. Paterson, S.R. Kirk, S. Jenkins, Response of the mechanical and chiral character of ethane to ultra-fast laser pulses, Journal of Computational Chemistry. Early View (2023). https://doi.org/10.1002/jcc.27225.
[8] H. Lu, A. Azizi, X. Mi, W. Yu, Y. Peng, T. Xu, H. Früchtl, T. van Mourik, S.R. Kirk, S. Jenkins, Scoring Molecular Wires Subject to an Ultra-Fast Laser Pulse for Molecular Electronic Devices, Journal of Computational Chemistry. 44 (2023) 1776–1785. https://doi.org/10.1002/jcc.27126.
[9] S.R. Kirk, S. Jenkins, Beyond energetic and scalar measures: Next generation quantum theory of atoms in molecules, WIREs Comput. Mol. Sci. 12 (2022) :10.1002/jcc.24358. https://doi.org/10.1002/wcms.1611.
[10] S.R. Kirk, S. Jenkins, Tools for overcoming reliance on energy-based measures in chemistry: a tutorial review, Chem. Soc. Rev. 52 (2023) 5861–5874. https://doi.org/10.1039/D3CS00350G.
[11] M.X. Hu, T. Xu, R. Momen, A. Azizi, S.R. Kirk, S. Jenkins, The normal modes of vibration of benzene from the trajectories of stress tensor eigenvector projection space, Chem. Phys. Lett. 677 (2017) 156–161. https://doi.org/10.1016/j.cplett.2017.04.017.
[12] W.J. Huang, T. Xu, S.R. Kirk, M. Filatov, S. Jenkins, QTAIM and stress tensor bond-path framework sets for the ground and excited states of fulvene, Chem. Phys. Lett. 713 (2018) 125–131. https://doi.org/10.1016/j.cplett.2018.10.029.
[13] J.H. Li, W.J. Huang, T. Xu, S.R. Kirk, S. Jenkins, Stress Tensor Eigenvector Following with Next-Generation Quantum Theory of Atoms in Molecules, Int. J. Quantum Chem. 119 (2018) e25847. https://doi.org/10.1002/qua.25847.
[14] H. Guo, A. Morales-Bayuelo, T. Xu, R. Momen, L. Wang, P. Yang, S.R. Kirk, S. Jenkins, Distinguishing and quantifying the torquoselectivity in competitive ring-opening reactions using the stress tensor and QTAIM, J. Comput. Chem. 37 (2016) 2722–2733. https://doi.org/10.1002/jcc.24499.
[15] P. Yang, T. Xu, R. Momen, A. Azizi, S.R. Kirk, S. Jenkins, Fatigue and photochromism S1 excited state reactivity of diarylethenes from QTAIM and the stress tensor, Int. J. Quantum Chem. 118 (2018) e25565. https://doi.org/10.1002/qua.25565.
[16] T. Xu, L. Wang, Y. Ping, T. van Mourik, H. Früchtl, S.R. Kirk, S. Jenkins, Quinone-based switches for candidate building blocks of molecular junctions with QTAIM and the stress tensor, Int. J. Quantum Chem. 118 (2018) e25676. https://doi.org/10.1002/qua.25676.
[17] T. Xu, J. Farrell, R. Momen, A. Azizi, S.R. Kirk, S. Jenkins, D.J. Wales, A Stress Tensor Eigenvector Projection Space for the (H2O)5 Potential Energy Surface, Chem. Phys. Lett. 667 (2017) 25–31. https://doi.org/10.1016/j.cplett.2016.11.028.
[18] P. Szarek, Y. Sueda, A. Tachibana, Electronic stress tensor description of chemical bonds using nonclassical bond order concept, J. Chem. Phys. 129 (2008) 094102. https://doi.org/10.1063/1.2973634.
[19] T. Tian, T. Xu, S.R. Kirk, I.T. Rongde, Y.B. Tan, S. Manzhos, Y. Shigeta, S. Jenkins, Intramolecular Mode Coupling of the Isotopomers of Water: A Non-Scalar Charge Density-Derived Perspective, Phys. Chem. Chem. Phys. 22 (2020) 2509–2520. https://doi.org/10.1039/C9CP05879F.
[20] V. Pohl, G. Hermann, J.C. Tremblay, An open-source framework for analyzing N-electron dynamics. I. Multideterminantal wave functions, Journal of Computational Chemistry. 38 (2017) 10.1002/jcc.24896. https://doi.org/10.1002/jcc.24792.
[21] G. Hermann, V. Pohl, J.C. Tremblay, An open-source framework for analyzing N-electron dynamics. II. Hybrid density functional theory/configuration interaction methodology, Journal of Computational Chemistry. 38 (2017) 2378–2387. https://doi.org/10.1002/jcc.24896.
[22] S. Giri, A.M. Dudzinski, J.C. Tremblay, G. Dixit, Time-dependent electronic current densities in chiral molecules, Phys. Rev. A. 102 (2020) 063103. https://doi.org/10.1103/PhysRevA.102.063103.
[23] T. Yanai, D.P. Tew, N.C. Handy, A new hybrid exchange–correlation functional using the Coulomb-attenuating method (CAM-B3LYP), Chemical Physics Letters. 393 (2004) 51–57. https://doi.org/10.1016/j.cplett.2004.06.011.
[24] R.A. Kendall, T.H. Dunning, R.J. Harrison, Electron affinities of the first-row atoms revisited. Systematic basis sets and wave functions, J. Chem. Phys. 96 (1992) 6796–6806. https://doi.org/10.1063/1.462569.

[25] T.H. Dunning, Gaussian basis sets for use in correlated molecular calculations. I. The atoms boron through neon and hydrogen, J. Chem. Phys. 90 (1989) 10.1021/acs.jctc.0c01228. https://doi.org/10.1063/1.456153.
[26] Michael J. Frisch, G. W. Trucks, *et. al*., Gaussian 09, Revision E.01, (2009). www.gaussian.com.
[27] R. Sarkar, M. Boggio-Pasqua, P.-F. Loos, D. Jacquemin, Benchmarking TD-DFT and Wave Function Methods for Oscillator Strengths and Excited-State Dipole Moments, J. Chem. Theory Comput. 17 (2021) 1117–1132. https://doi.org/10.1021/acs.jctc.0c01228.
[28] G. Hermann, V. Pohl, J.C. Tremblay, B. Paulus, H.-C. Hege, A. Schild, ORBKIT: A modular python toolbox for cross-platform postprocessing of quantum chemical wavefunction data, Journal of Computational Chemistry. 37 (2016) 1511–1520. https://doi.org/10.1002/jcc.24358.
[29] Y. Zhu, J.M. Herbert, Self-consistent predictor/corrector algorithms for stable and efficient integration of the time-dependent Kohn-Sham equation, The Journal of Chemical Physics. 148 (2018) 044117. https://doi.org/10.1063/1.5004675.
[30] Y. Zhu, J.M. Herbert, High harmonic spectra computed using time-dependent Kohn–Sham theory with Gaussian orbitals and a complex absorbing potential, The Journal of Chemical Physics. 156 (2022) 204123. https://doi.org/10.1063/5.0079910.
[31] S. Klinkusch, J.C. Tremblay, Resolution-of-identity stochastic time-dependent configuration interaction for dissipative electron dynamics in strong fields, The Journal of Chemical Physics. 144 (2016) 184108. https://doi.org/10.1063/1.4948646.
[32] G. Hermann, J.C. Tremblay, Ultrafast photoelectron migration in dye-sensitized solar cells: Influence of the binding mode and many-body interactions, The Journal of Chemical Physics. 145 (2016) 174704. https://doi.org/10.1063/1.4966260.
[33] G. Füchsel, J.C. Tremblay, T. Klamroth, P. Saalfrank, Selective Excitation of Molecule-Surface Vibrations in H2 and D2 Dissociatively Adsorbed on Ru(0001), Israel Journal of Chemistry. 52 (2012) 438–451. https://doi.org/10.1002/ijch.201100097.
[34] I. Tutunnikov, E. Gershnabel, S. Gold, I.Sh. Averbukh, Selective Orientation of Chiral Molecules by Laser Fields with Twisted Polarization, J. Phys. Chem. Lett. 9 (2018) 1105–1111. https://doi.org/10.1021/acs.jpclett.7b03416.
[35] I. Tutunnikov, J. Floß, E. Gershnabel, P. Brumer, I.Sh. Averbukh, A.A. Milner, V. Milner, Observation of persistent orientation of chiral molecules by a laser field with twisted polarization, Phys. Rev. A. 101 (2020) 10.1016/j.cpc.2013.10.026. https://doi.org/10.1103/PhysRevA.101.021403.
[36] A. Otero-de-la-Roza, E.R. Johnson, V. Luaña, Critic2: A program for real-space analysis of quantum chemical interactions in solids, Computer Physics Communications. 185 (2014) 1007–1018. https://doi.org/10.1016/j.cpc.2013.10.026.
[37] A. Otero-de-la-Roza, Finding critical points and reconstruction of electron densities on grids, The Journal of Chemical Physics. 156 (2022) 224116. https://doi.org/10.1063/5.0090232.
[38] S.R. Kirk, S. Jenkins, QuantVec, (2021). DOI.org/10.5281/zenodo.5553686 (accessed October 7, 2021).
[39] Z. Li, T. Xu, H. Früchtl, T. van Mourik, S.R. Kirk, S. Jenkins, Mixed Chiral and Achiral Character in Substituted Ethane: A Next Generation QTAIM Perspective, Chem. Phys. Lett. 803 (2022) 10.1021/jacs.0c05128. https://doi.org/10.1016/j.cplett.2022.139762.